# Magnetic Resonance Study of a Series of Phosphorus-Containing Zintl Compounds: $Ca_{14}AlP_{11}$, $Ca_{14}MnP_{11}$, and $Eu_{14}MnP_{11}$

Eva Ratai, Paul Bruins, Carlos J. Hernandez, Susan M. Kauzlarich,* and Matthew P. Augustine*

*Department of Chemistry, University of California Davis, One Shields Avenue, Davis, California 95616*

*Received August 24, 2001. Revised Manuscript Received January 3, 2002*

The compounds $Ca_{14}AlP_{11}$, $Ca_{14}MnP_{11}$, and $Eu_{14}MnP_{11}$ have been synthesized and are isostructural to the Zintl compound, $Ca_{14}AlSb_{11}$. $Eu_{14}MnP_{11}$ is a ferromagnet showing colossal magnetoresistance at $T_C = 52$ K, $Ca_{14}MnP_{11}$ shows paramagnetic behavior down to 5 K, and $Ca_{14}AlP_{11}$ is nonmagnetic. The formula unit for these Zintl compounds is $A_{14}MPn_{11}$ and comprises 14 A cations, a $MPn_4$ tetrahedron, four isolated Pn anions, and a $Pn_3$ linear unit. The central Pn of the $Pn_3$ unit is believed to be positionally disordered, and it has been speculated that the disorder is static rather than dynamic. To address this issue, $^{31}P$ solid-state NMR was applied to these new compounds to provide insight into the magnetic ordering and structural changes. The NMR chemical shift anisotropy and the dipolar coupling for the $^{31}P$ nuclei as well as the quadrupolar coupling for the $^{27}Al$ nucleus in the diamagnetic compound $Ca_{14}AlP_{11}$ provide structural details consistent with the Zintl structure. Wide-line $^{31}P$ NMR and EPR were applied to the paramagnetic compounds $Ca_{14}MnP_{11}$ and $Eu_{14}MnP_{11}$ to obtain similar structural information. The lack of any EPR spectra for the Eu-substituted compound below 50 K confirms the assigned paramagnetic-to-ferromagnetic transition temperature of 52 K. Hyperfine couplings in the Eu-substituted compound suggests localization of the electron density above 50 K.

## Introduction

Magnetoresistive materials are the active components of magnetic field sensors and read heads for computer hard drives because of their displayed dependence of electric resistance on magnetic field.[1,2] The structure of one class of these materials can be rationalized by the Zintl−Klemm concept.[3−5] These so-called Zintl compounds contain electropositive electron donors and electronegative electron acceptors. The electropositive elements donate their electrons to the electronegative elements, thus supporting the formation of polyatomic anions and anionic networks. This charge-transfer process is a critical ingredient in the Zintl−Klemm structure that allows formation of stoichiometric charge precise compounds. As an example of the Zintl−Klemm concept, consider the structure of the compound $A_{14}MPn_{11}$ shown in Figure 1 where A, M, and Pn represent a positive divalent ion, a positive trivalent ion, and a pnictogen, respectively. One formula unit of this material contains 14 $A^{2+}$ cations, one $MPn_4^{9-}$ tetrahedron, four $Pn^{3-}$ anions, and one linear trimer $Pn_3^{7-}$.[6] The $MPn_4^{9-}$, $Pn^{3-}$, and linear trimer units are shown with $A^{2+}$ counterions in Figure 2 parts a−c, respectively. Although formal charge has been assigned to these building blocks, one must keep in mind that such an assignment may be too restrictive to describe the real bonding in the solid as a whole.

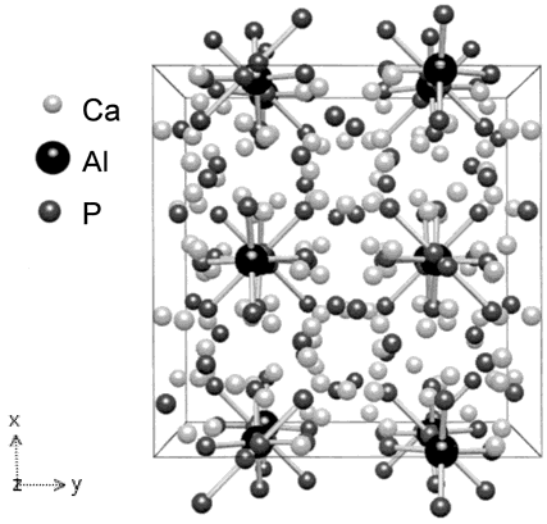


**Figure 1.** Unit cell showing the Zintl structure for $Ca_{14}AlP_{11}$. (The disordered site for the $P_3$ unit is shown as two spheres slightly displaced from the center of the $P_3$ unit.)

To date, the functional and structural characteristics of these Zintl compounds have been primarily ac-

(1) Brig, J.; Anthony, T. C.; Nickel, J. *MRS Bull.* **1996**, *21*, 23.
(2) Daughton, J. M. *J. Magn. Magn. Mater.* **1999**, *192*, 334.
(3) Schäfer, H.; Eisenmann, B.; Müller, W. *Angew. Chem., Int. Ed. Engl.* **1973**, *12*, 604.
(4) Schäfer, H.; Eisenmann, B. *Rev. Inorg. Chem.* **1981,** *3*, 29.
(5) Schäfer, H. *J. Solid State Chem.* **1985,** *57*, 97.
(6) Cordier, G.; Schäfer, H.; Stelter, M. *Z. Anorg. Allg. Chem.* **1984,** *519*, 183.

10.1021/cm010809q CCC: $22.00 
Published on Web 05/15/2002

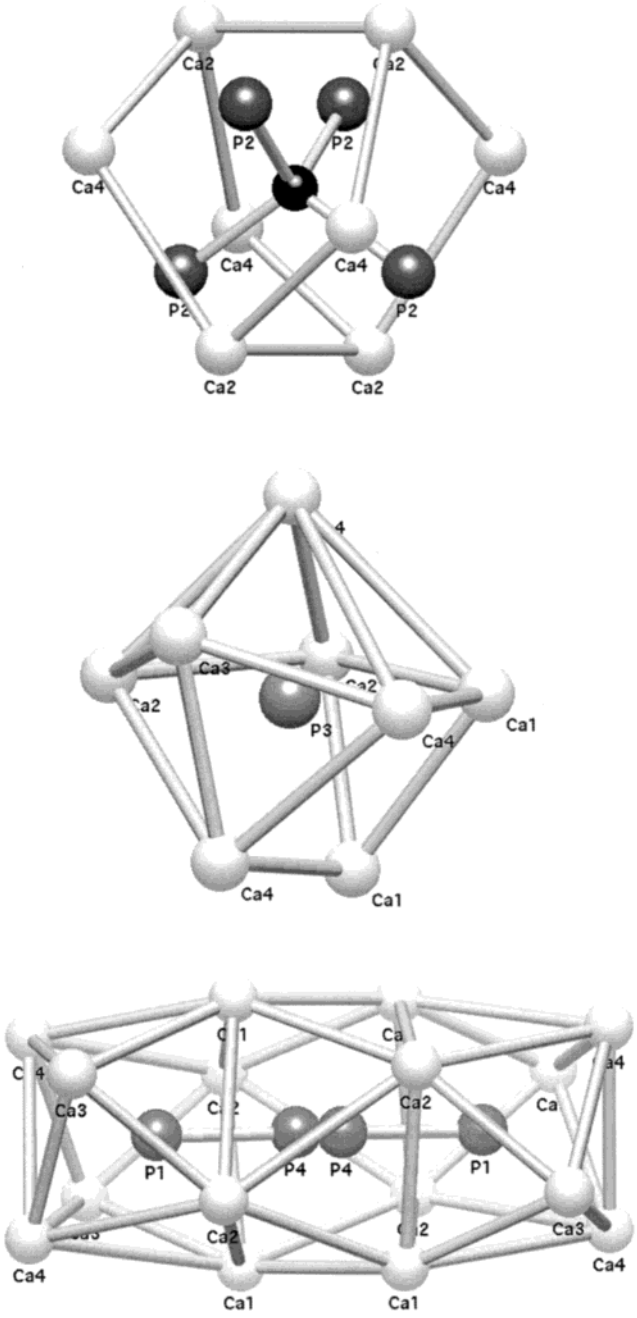


**Figure 2.** Three-dimensional view of the four Pn sites in the Zintl structure. The $MPn_4^{9-}$ tetrahedron in part a comprises the P2 site and the isolated P3 site is in the center of a monocapped octahedron of $M^{2+}$ ions in part b. The linear anion labels the P1 and P4 sites in part c. The structure in part c describes the P4 site as disordered, although the NMR data suggests a linear trimer.

complished by magnetism and diffraction measurements.[7−12] For example, the compound $Eu_{14}MnP_{11}$ undergoes a paramagnetic-to-ferromagnetic transition at 52 K and displays a magnetoresistance ratio MR % = $(\rho(H = 0\ \text{T}) - \rho(H = 5\ \text{T}))/\rho(H = 5\ \text{T}) \times 100 = 1.2 \times 10^5$% near the transition temperature.[13] Here $\rho(H)$ is the measured resistance at different magnetic fields, $H$. Although adequate for bulk structural comparisons, the magnetism and diffraction techniques cannot answer atomic scale questions. For example, the valence state of the Mn ion in the $MPn_4^{9-}$ tetrahedron in these compounds is currently under scrutiny. While the measured magnetic moment of approximately $4\mu_B$/Mn suggests that the valence state is 3+,[14] theoretical work on $Ca_{14}MnBi_{11}$ and $Ba_{14}MnBi_{11}$ identifies the Mn ion as having a $d^5$ configuration, consistent with a +2 charge for Mn.[15] This model has been confirmed in the case of $Yb_{14}MnSb_{11}$.[16] For the Bi compounds, the theoretical analysis suggests that a hole resides on the Bi of the $MnBi_4$ tetrahedron thus producing a moment lower than expected for $Mn^{2+}$. Another atomic scale question regards the $Pn_3^{7-}$ unit that has 22 valence electrons and is isostrutural to $I_3^-$. Ab initio calculations for this moiety in the compound $Ca_{14}GaAs_{11}$ have supported the idea of a three centered, four-electron bond.[17] Single-crystal X-ray data on the other hand suggest a split position for the central Pn atom with 50% occupation on each site.[18] Raman and IR data on the compound $Ba_{14}InP_{11}$ support the model of a dimer−monomer combination where $P_2^{4-}$ and a weakly associated $P^{3-}$ are involved instead of the presence of a four-electron bond.[19]

Although the synthesis and examination of the magnetic properties of these powdered solid materials are straightforward, there have been no magnetic resonance studies directed at unraveling the relationship between chemical structure modification and magnetoresistance. In an attempt to better understand the structure and bonding in Zintl solids on the atomic scale, nuclear magnetic resonance (NMR) and electron paramagnetic resonance (EPR) were applied to the isostructural series of compounds $Ca_{14}AlP_{11}$, $Ca_{14}MnP_{11}$, and $Eu_{14}MnP_{11}$. Besides containing the NMR active $^{31}P$ isotope, these three compounds have the additional feature of spanning the full magnetism range. At all temperatures measured, the compound $Ca_{14}AlP_{11}$ is diamagnetic and the compound $Ca_{14}MnP_{11}$ is paramagnetic while, as mentioned above, the $Eu_{14}MnP_{11}$ compound undergoes a paramagnetic-to-ferromagnetic transition at 52 K.

To understand the site-specific electronic asymmetry in this class of new compounds, $^{31}P$ magic angle spinning (MAS) NMR was applied to the diamagnetic compound $Ca_{14}AlP_{11}$. The envelope of the measured spinning sideband pattern was used in conjunction with computer simulation to extract the site-specific chemical

(7) Kauzlarich, S. M. In *Transition Metal Zintl Compounds*; Kauzlarich, S. M., Ed.; VCH Publishers: New York, 1996; p 245.
(8) Rehr, A.; Kuromuoto, T. Y.; Kauzlarich, S. M.; Del Castillo, J.; Webb, D. J. *Chem. Mater.* 1994, *6*, 93.
(9) Kuromuoto, T. Y.; Kauzlarich, S. M.; Webb, D. J. *J. Am. Chem. Soc.* **1992**, *4*, 435.
(10) Brock, S. L.; Weston, L. J.; Olmstead, M. M.; Kauzlarich, S. M. *J. Solid State Chem.* **1993**, *107*, 513.
(11) Chan, J. Y.; Kauzlarich, S. M.; Klavins, P.; Shelton, R. N.; Webb, D. J. *Chem. Mater.* **1997**, *9* 3132.
(12) Chan, J. Y.; Kauzlarich, S. M.; Klavins, P.; Shelton, R. N.; Webb, D. J. *Phys. Rev. B* **1998**, *57*, 8103.
(13) Payne, A. C.; Olmstead, M. M.; Kauzlarich, S. M.; Webb, D. J. *Chem. Mater.* **2001,** *13*, 1398.
(14) Fischer, I. R.; Wiener, T. A.; Bud'ko, L. S.; Canfield, P. C.; Chan, J. Y.; Kauzlarich, S. M. *Phys. Rev. B* **59 1999**, 13829.
(15) Sánchez-Portal, D.; Martin, R. M.; Kauzlarich, S. M.; Pickett, W. E.; *Phys. Rev. B.*, submitted for publication.
(16) Holm, A. P.; Kauzlarich, S. M.; Morton, S. A.; Waddill, G. D.; Pickett, W. E.; Tobin, J. J. *J. Am. Chem. Soc.*, submitted for publication.
(17) Gallup, R. F.; Fong, C.; Kauzlarich, S. M. *Inorg. Chem.* **1992**, *31* 115.
(18) Vaughey, J. T.; Corbett, J. D. *Chem. Mater.* **1996**, *8* 671.
(19) Carrillo-Cabrera, W.; Somer, M.; Peters, K.; van Schnering, H. G. *Chem. Ber.* **1996**, *129*, 1015.

shift anisotropy (CSA) for each of the separate phosphorus sites in $Ca_{14}AlP_{11}$. The three CSA principal values directly correspond to directions and magnitudes of electron density at a particular P site. The distances between the various P sites in the Zintl structure suggests the presence of homonuclear $^{31}P$ dipolar couplings in these three compounds. An estimate of the size of these couplings by comparison of $^{31}P$ spin echo decay rates with and without MAS yields distance information for the powdered solid[20] that can be compared to X-ray data. Another probe of the structure in the $Ca_{14}AlP_{11}$ compound is the $^{27}Al$ nucleus. The NMR spectra of $^{27}Al$ in the solid state at different magnetic fields can be used to estimate the quadrupolar coupling constant, a number that also relates to electronic asymmetry in the $Ca_{14}AlP_{11}$ compound.

Unfortunately, application of the same MAS NMR techniques to the Mn-substituted compound $Ca_{14}MnP_{11}$ failed. The presence of the paramagnetic Mn ion broadens the $I = {}^1/_2$ solid state $^{31}P$ spectra beyond the bandwidth of conventional pulsed NMR spectrometers. To probe the extremely broad NMR spectra for this material, a field swept NMR spectrometer based on the work of Wu et al. was developed.[21] This approach permitted both the accumulation of necessary one-dimensional $^{31}P$ NMR spectra for $Ca_{14}MnP_{11}$ and an automated measurement of the spin lattice relaxation time $T_1$ across the whole NMR line. These $T_1$ values are used to determine the resonance frequency for the various $^{31}P$ sites in $Ca_{14}MnP_{11}$.

Finally, continuous wave EPR was applied to the paramagnetic compounds $Ca_{14}MnP_{11}$ and $Eu_{14}MnP_{11}$ (above 50 K) to provide further insight into the electronic properties of the 14−1−11 structure.

## Experimental Section

**Synthesis.** The compounds $Ca_{14}AlP_{11}$ and $Ca_{14}MnP_{11}$ were prepared by heating stoichiometric amounts of the elements in Nb tubes for 5 days at 1050 °C in a furnace. Detailed synthesis and characterization of the transport properties of these compounds can be found in an another publication.[22] The rare-earth-metal-substituted $Eu_{14}MnP_{11}$ was synthesized from stoichiometric amounts of Eu and P with a 2-fold excess of Mn as previously described.[13] In this case, the reaction was performed by heating the mixture in a Ta ampule for 7 days at 1250 °C. All reactants and products were handled in a nitrogen-filled drybox.

**X-ray Powder Diffraction.** X-ray powder diffraction measurements were performed with an Enraf-Nonius camera (Cu $K\alpha_1$ radiation). The sample was mixed with 10% NBS Si standard, mounted between two pieces of cellophane tape, and finally moved into a vacuum chamber connected to the camera. Film data were then compared to the powder pattern calculated from previously obtained single-crystal measurements. The diffraction pattern for the powdered reaction mixtures compare well with single-crystal data for $Ca_{14}MnP_{11}$[22] and $Eu_{14}MnP_{11}$.[13] Single-crystal data were not available for $Ca_{14}AlP_{11}$. The powder diffraction pattern could be indexed according to the $Ca_{14}AlSb_{11}$ structure type.

**Solid-State NMR.** All $^{31}P$ MAS measurements were recorded at 119.55 MHz using a home-built NMR spectrometer constructed around an Oxford Instruments 6.95 T superconducting magnet and controlled by a Tecmag Orion pulse programmer. The high spinning speed (8−20 kHz) $^{31}P$ MAS spectra were obtained with a Chemagnetics MAS probe configured for rotors having an outer diameter of 3.5 mm. The samples were packed into zirconium oxide rotors in a drybox and spun with dry $N_2$ gas. The low spinning speed (1.6−7 kHz) $^{31}P$ MAS spectra were obtained with a Chemagnetics MAS probe equipped for 7.5 mm o.d. rotors having O-ring sealed PTFE plugs. All spectra were acquired with a rotor synchronized spin echo pulse sequence with typical 90° pulse lengths of 7 $\mu$s and relaxation delays of 1−2 s. Chemical shifts were externally referenced to $H_3PO_4$ (85%) and the principal values of the chemical shift tensors were obtained by regressing the MAS spectra to simulations performed using the Herzfeld−Berger approach.[23] Estimates of the $^{31}P-^{31}P$ homonuclear dipolar coupling in $Ca_{14}AlP_{11}$ were accomplished by tracking the decay of the spin echo amplitude with and without MAS as a function of pulse spacing between 25 $\mu$s and 1 ms. $^{27}Al$ NMR spectra for $Ca_{14}AlP_{11}$ were obtained at Larmor frequencies of 76.97 MHz using the spectrometer described above and at 104.25 MHz using a Chemagnetics CMX-400 spectrometer equipped with a 7.5 mm o.d. MAS probe. All spectra were reference to an $Al(NO_3)_3$ solution. Static $^{27}Al$ NMR spectra were acquired with a spin echo pulse sequence with typical 90° pulse lengths of 5 $\mu$s and relaxation delays of 200 ms, while MAS spectra were measured with single pulse excitation using short 2 $\mu$s pulses.

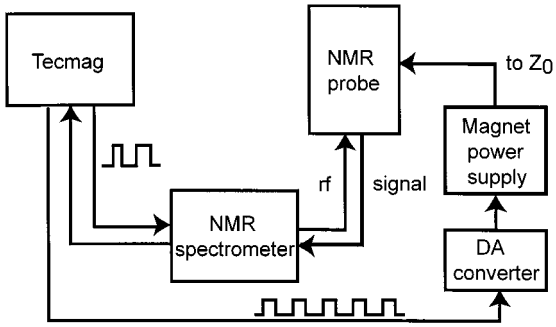


**Figure 3.** Block diagram of the wide line NMR spectrometer used in this study.

**Wide-Line NMR.** Static $^{31}P$ NMR spectra of the paramagnetic compound $Ca_{14}MnP_{11}$ were measured at 107.17 MHz using a home-built NMR spectrometer constructed around a Nalorac Cryogenics Corp. 6.22 T magnet and controlled by a Tecmag Libra pulse programmer. To measure the entire $^{31}P$ NMR spectrum of this paramagnetic solid, a broadband field swept apparatus was developed based on the work of Wu et al.[21] The probe head has a $Z_0$ coil consisting of approximately 3000 turns of 28 gauge square magnet wire wrapped on a 20 mm quartz tube. The outside diameter of this 100 mm long field sweep coil is 40 mm. The coil resistance was measured to be 40 Ω, which when impedance matched to an HP 6655A programmable 120 V power supply, allows currents up to 4 A to be applied to the $Z_0$ coil corresponding to up to a 1 kG magnetic field. A water-cooled jacket encasing this $Z_0$ coil provides necessary cooling when sweeping fields greater than 100 G. The HP 6655A power supply is controlled with an externally provided 0−5 V analogue reference signal generated by a home-built interface connected to a Tecmag Libra data acquisition system. The interface primarily consists of a 16 bit digital to analog converter that derives its input from TTL level gating pulses and the Tecmag sense control via four 4-bit cascaded ripple counters. The 16-bit resolution of the circuit allows field increments of 150 mG. Finally, an eight turn 6 mm diameter 12 mm long solenoid coil with long axis perpendicular to and mounted inside of the $Z_0$ coil completes a tank circuit for excitation and detection of NMR.

Figure 3 shows the basic building blocks of the wide-line NMR setup. The data were collected by varying the magnetic

(20) Lathrop, D.; Franke, D.; Maxwell, R.; Tepe, T.; Fleshe, R.; Zhang, Z.; Eckert, H. *Solid State Magn. Reson.* **1992,** *1*, 73.

(21) Wu, Patterson, D. A.; Butler, L. G.; Miller, J. B. *Rev. Sci. Instrum.* **1993**, *64*, 1235.

(22) Kim, H.; Ratai, E.; Augustine, M. P.; Kauzlarich, S. M. Manuscript in preparation.

(23) Herzfeld, J.; Berger, A. E. *J. Chem. Phys.* **1980**, *73*, 6021.

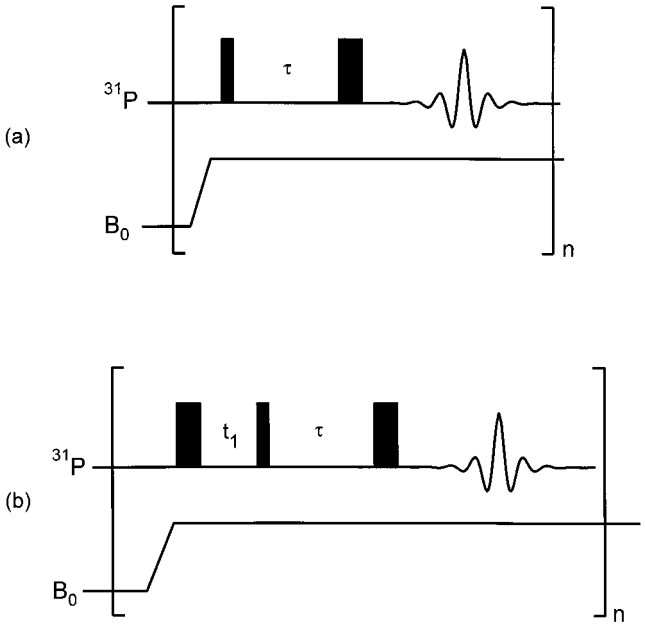


**Figure 4.** Pulse sequences used to obtain wide line $^{31}$P NMR spectra in part a and measure spin lattice relaxation times in part b for the paramagnetic solids in this study.

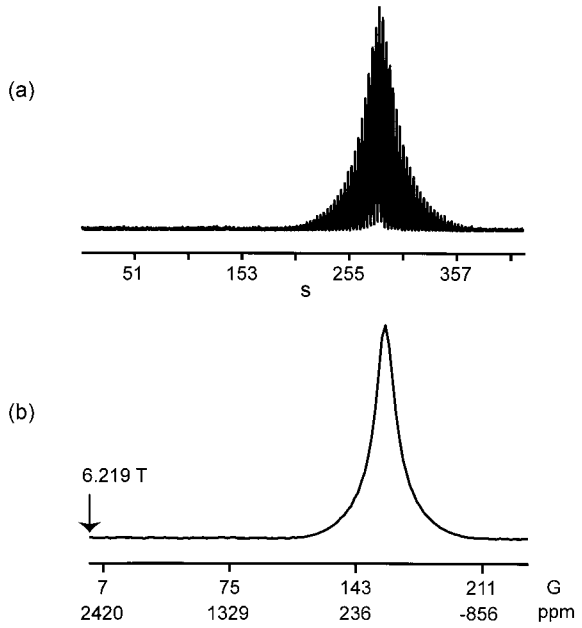


**Figure 5.** Spin echoes observed in liquid $H_3PO_4$ (85%) using the field swept apparatus in Figure 3 and the pulse sequence in Figure 4a. The time $t = 0$ in part a corresponds to the beginning of the field sweep. The maximum of each echo in part a corresponds to a measured spectral point in part b as a function of both field and ppm.

field in the sweep coil from 0 to 470 G in steps of 1.8 G, using a spin echo pulse sequence. Typically 90° pulse lengths of 5 $\mu$s, pulse delays of $\tau = 200$ ms, and relaxation delays of 3 s are used as shown in Figure 4a. An example of the performance of this apparatus for an applied frequency of 107.4 MHz from 0 to 236 G is shown in Figure 5 for liquid $H_3PO_4$ (85%). The data shown in Figure 5a displays the absolute value of the real and imaginary parts of the spin echoes accumulated with the pulse sequence in Figure 4a. The spectrum constructed Figure 5b corresponds to a plot of the maximum of each of the spin echoes in Figure 5a as a function of magnetic field. The same field sweeping apparatus was used to measure the spin lattice relaxation time $T_1$, across the $Ca_{14}MnP_{11}$ NMR

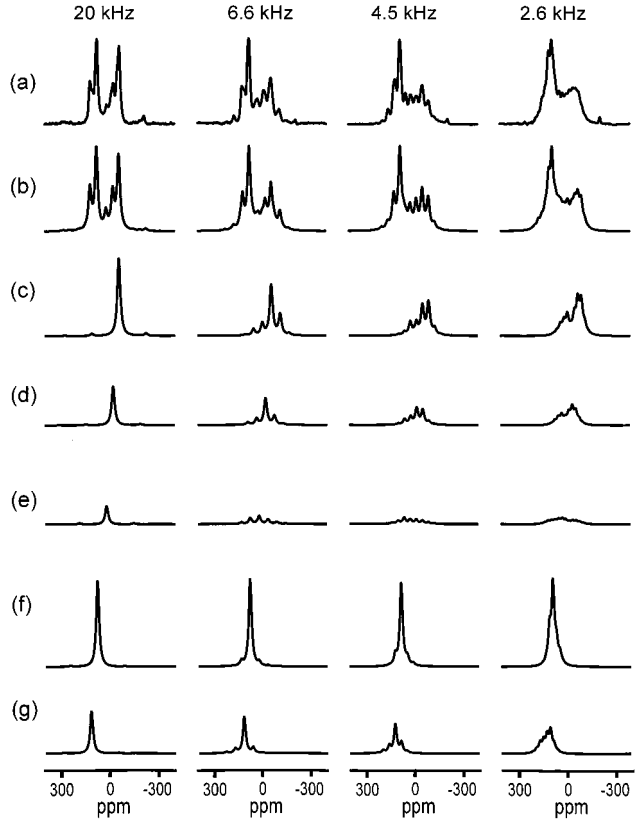


**Figure 6.** (a) Summary of $^{31}$P MAS NMR spectra as a function of spinning speed for the compound $Ca_{14}AlP_{11}$. The simulations in part b correspond to a five site model. The intensity and principal values of the CSA tensor for each of these sites is provided in Table 1, and the subspectra in parts c−g correspond to these values.

line using the pulse sequence shown in Figure 4b. Typically, $t_1$ time increments vary from 10 $\mu$s to 5 s in Figure 4b.

**EPR.** Continuous wave EPR spectra for the compounds $Ca_{14}AlP_{11}$, $Ca_{14}MnP_{11}$, and $Eu_{14}MnP_{11}$ were measured with a Bruker CS 106 X-band EPR spectrometer equipped with a Bruker ER 4116DM dual mode cavity capable of both perpendicular (TE102) and parallel (TE012) mode polarizations of the applied electromagnetic field. An Oxford ESR900 liquid helium cryostat controlled by an Oxford ITC503 flow regulator was used to obtain cryogenic temperatures down to 25 K.

## Results

The $^{31}$P MAS NMR spectra for $Ca_{14}AlP_{11}$ as a function of spinning speed between 2.6 and 20 kHz are shown in Figure 6a. These spectra are best fit with a five site model using the Herzfeld−Berger approach for each site as shown in Figure 6b. The individual CSA MAS patterns for each of the five sites with proper intensity are shown in Figure 6, parts c−g. The relative intensity of each of these MAS spectra, the principal values for the CSA tensor, and the isotropic shift for each site in Figure 6, parts c−g, are included in Table 1.

The solid triangles and solid diamonds in Figure 7 correspond to the decay of the $^{31}$P spin echo for $Ca_{14}AlP_{11}$ with and without rotor synchronized MAS, respectively. The time $\tau$ refers to the spacing of the 90 and 180° pulses in the spin echo pulse sequence; therefore, the maximum of the spin echo occurs at the time $2\tau$. The dashed line corresponds to the Gaussian decay expected when $^{31}$P−$^{31}$P dipolar couplings in the $Ca_{14}AlP_{11}$ structure are admitted.

**Table 1. Relative Intensity and CSA Principal Values for the Different P Sites in $Ca_{14}AlP_{11}$[a,b]**

| | peak 1 | peak 2 | peak 3 | peak 4 | peak 5 |
|---|---|---|---|---|---|
| intensity | 4 | 2 | 1 | 4 | 2 |
| $\delta_{xx}$ | 3 | 48 | 112 | 106 | 176 |
| $\delta_{yy}$ | −20 | 3 | −0.5 | 78 | 131 |
| $\delta_{zz}$ | −158 | −114 | −50 | 53 | 50 |
| $\delta_{iso}$ | −58 | −21 | 21 | 79 | 119 |
| $\delta$ | −150 | −140 | 137 | 41 | −69 |
| $\eta$ | 0.2 | 0.5 | 0.6 | 0.9 | 0.7 |

[a] Units of $\delta$ are ppm. [b] For a definition of $\delta$ and $\eta$ in terms of the $\delta_{nn}$ see ref 33. Peaks 1−5 correspond to the subspectra c−g in Figure 6.

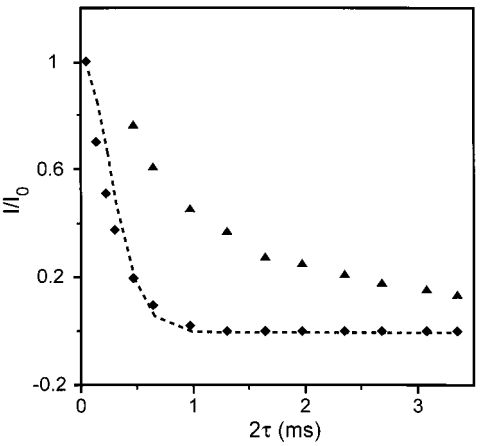


**Figure 7.** Decay of the $^{31}P$ spin echo signal for all sites in $Ca_{14}AlP_{11}$ with and without MAS. The solid triangles correspond to the decay with 5 kHz rotor synchronized MAS while the solid diamonds represent the decay of a static sample. The dashed line is the Gaussian decay of magnetization due to $^{31}P-^{31}P$ dipolar coupling in the static sample.

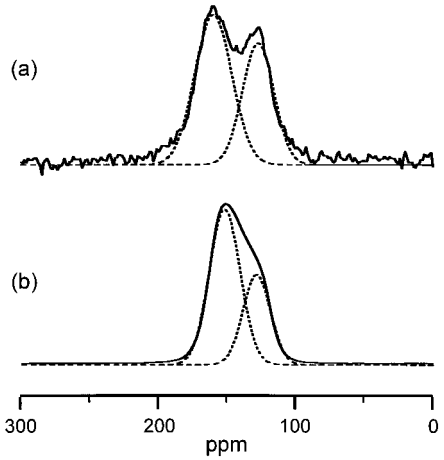


**Figure 8.** Static $^{27}Al$ NMR spectra of $Ca_{14}AlP_{11}$ at (a) 7.04 and (b) 9.4 T. The inset dashed lines correspond to two Gaussian peaks used to reasonably accurately determine the frequency positions of the powder pattern singularities.

The $^{27}Al$ NMR spectra of $Ca_{14}AlP_{11}$ without MAS at 6.95 and 9.4 T are shown in Figure 8, parts a and b, respectively. The peaks of the obvious quadrupolar doublet at 6.95 T are split by 32.8 ppm. The higher field truncates the quadrupolar effect thus scaling the splitting to 23.3 ppm at 9.4 T in Figure 8b. The quadrupolar splittings in both parts a and b of Figure 8 were determined by fitting the spectra to two Gaussian peaks as shown by the dashed lines.

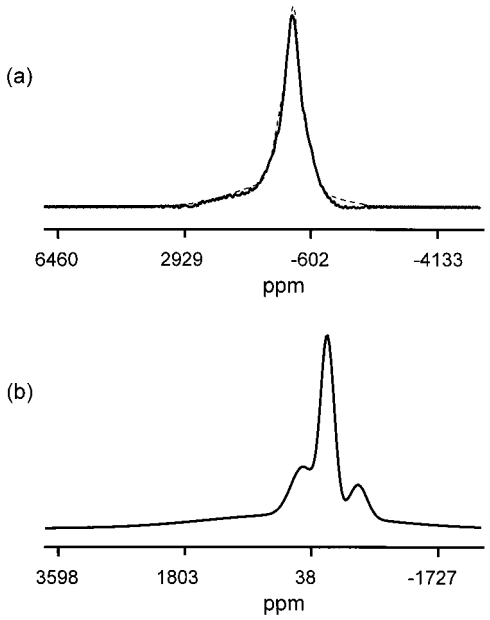


**Figure 9.** Wide line $^{31}P$ NMR spectra of the $Ca_{14}MnP_{11}$ compound obtained using the apparatus in Figure 3 and the pulse sequence in Figure 4a. The solid line in part a is the measured raw data and the dashed line is the convolution of the synthetic spectrum in part b with the rf excitation bandwidth described by the spectrum in Figure 5b. The synthetic spectrum in part b is the sum of four Gaussians whose parameters are listed in Table 2.

The stepped field experiment was used to measure the static $^{31}P$ NMR spectrum of the paramagnetic compound $Ca_{14}MnP_{11}$. The raw $^{31}P$ NMR spectrum obtained with the stepped field apparatus is shown as the solid line in Figure 9a. This spectrum is the convolution of the true static $^{31}P$ NMR spectrum for $Ca_{14}MnP_{11}$ with the rf excitation profile. The severity of this artificial externally imposed line broadening mechanism can be appreciated with reference to the 195 ppm wide $^{31}P$ NMR spectrum for liquid $H_3PO_4$ shown in Figure 5b. The lifetime broadened line width for $H_3PO_4$ in a well shimmed magnet is on the order of 1 Hz $\sim$ 0.01 ppm, therefore the spectrum in Figure 5b with line width dominated by the rf excitation can be used to deconvolute the spectrum in Figure 9a. Since deconvolution algorithms are extremely sensitive to nonlinearities in input spectra like noise, the measured spectrum was calculated by convolving a synthetic spectrum composed of Gaussian basis functions with the rf excitation bandwidth function in Figure 5b. The difference between the measured data in Figure 9a and the convolved function was minimized by varying the number, position, width, and intensity of Gaussian functions in the synthetic spectrum. The synthetic spectrum that yields the best agreement with the measured data involves just four Gaussian basis functions and is shown in Figure 9b. Convolution of this function with the spectrum in Figure 5b yields the dashed line in Figure 9a. The intensity, position, and width of the four Gaussian basis functions used to construct Figure 9b are provided in Table 2. The spin lattice relaxation time $T_1$ for these four sites in $Ca_{14}MnP_{11}$ is also included in Table 2. These $T_1$ values were obtained with the stepped field inversion recovery pulse sequence shown in Figure 4b. An example of the

**Table 2. Positions, Widths, and $T_1$ Values for the Different P Sites in $Ca_{14}MnP_{11}$**

| | peak 1 | peak 2 | peak 3 | peak 4 |
|---|---|---|---|---|
| intensity | 1 | 4 | 2 | 4 |
| $\delta_{iso}$[a] | −612 | −159 | 195 | 335 |
| fwhm[a] | 292 | 223 | 407 | 2850 |
| $T_1$[b] | 454 | 2.9 | 1.4 | 0.7 |

[a] Units are ppm. [b] Units are ms.

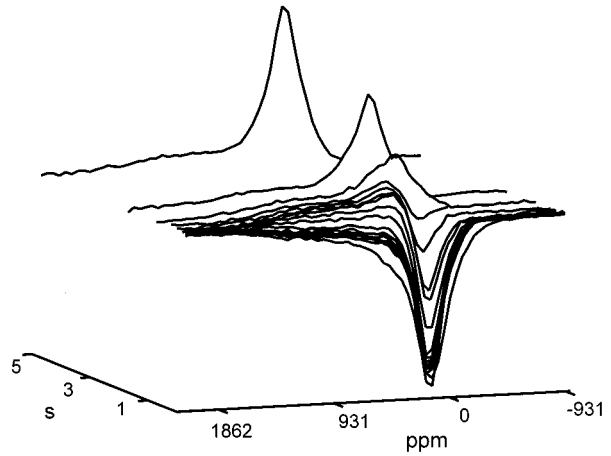


**Figure 10.** Wide line $^{31}P$ $T_1$ measurement of the $Ca_{14}MnP_{11}$ compound obtained using the apparatus in Figure 3 and the pulse sequence in Figure 4b. The relaxation naturally separates into the four spectral regions indicated by the times in Table 2.

raw $^{31}P$ spectral data for $Ca_{14}MnP_{11}$ is shown in Figure 10.

The EPR spectra for $Ca_{14}MnP_{11}$ and $Eu_{14}MnP_{11}$ at 9.67 GHz as a function of temperature are shown in Figure 11, parts a and b, respectively. $Ca_{14}AlP_{11}$ showed no signal, as expected. Regardless of the temperature down to 25 K, the position and full width at half-height for the EPR line for $Ca_{14}MnP_{11}$ in Figure 11a are fixed at 3450 and 31 G respectively. The shape and position of the EPR line for $Eu_{14}MnP_{11}$ shown in Figure 11b are temperature dependent. In fact, the EPR spectrum completely disappears below 49 K, consistent with the 52 K magnetoresistance measurement of the paramagnetic−ferromagnetic transition. The EPR spectra for $Eu_{14}MnP_{11}$ at 51 and 49 K display fine structure that can be used to determine a hyperfine coupling of 374 G. The numerical derivative of these two spectra yields three lines at 51 K and six lines at 49 K.

## Discussion

Before proceeding with a comparison between the magnetic resonance measurements described above and structure, consider the X-ray results for $Ca_{14}AlP_{11}$. The entire Zintl family of compounds crystallizes in the body-centered tetragonal space group $I_1/acd$, with eight formula units (208 atoms). As mentioned above, one formula unit for $A_{14}MPn_{11}$ consists of 14 $A^{2+}$ cations on four inequivalent sites, a compressed $MPn_4^{9-}$ tetrahedron, four "isolated" $Pn^{3-}$ anions, and a linear anion $Pn_3^{7-}$. These three structural motifs are shown in Figure 2 and are referred to as the P2, P3, P1, and P4 sites, respectively. The P1 and P4 sites comprise the linear anion as shown in Figure 2c, and it is not known whether the P1 sites are equivalent as in the case of a linear trimer or inequivalent as in the case of a monomer−dimer combination. From the perspective of the NMR results in $Ca_{14}AlP_{11}$, it is important to note that the shortest $^{31}P-^{31}P$ distances are in the linear anion. Assuming a monomer−dimer combination the shorter P1−P4 distance is 2.517 Å and the longer P4−P1 distance is 3.337 Å. These X-ray-based measurements along with other useful P−P distances are listed in Table 3 for $Ca_{14}AlP_{11}$. The bond distances are calculated from the room-temperature lattice parameters for $Ca_{14}AlP_{11}$ of $a$ = 15.331 Å and $c$ = 20.759 Å assuming that it is isostructural with $Ca_{14}MnP_{11}$. To interpret the wide line $^{31}P$ NMR data in the $Ca_{14}MnP_{11}$ compound, it is useful to have the distances between

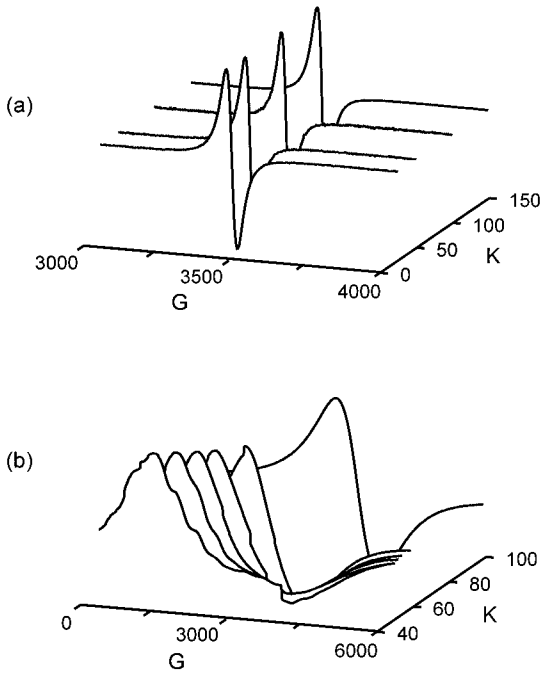


**Figure 11.** Variable temperature EPR spectra of the $Ca_{14}MnP_{11}$ compound (a) and the $Eu_{14}MnP_{11}$ compound (b). The EPR spectrum for the paramagnetic $Ca_{14}MnP_{11}$ compound in part a is temperature independent down to 25 K while the EPR spectra for the $Eu_{14}MnP_{11}$ compound near 52 K paramagnetic−ferromagnetic transition temperature in part b display a 374 G hyperfine coupling.

**Table 3. Useful P−P Distances in the Compound $Ca_{14}AlP_{11}$**

| pair | distance[a] |
|---|---|
| P1−P4 | 2.517 |
| P1−P4 | 3.337 |
| P1−P3 | 4.192 |
| P1−P2 | 4.252 |
| P1−P2 | 4.267 |
| P1−P3 | 4.533 |
| P1−P3 | 4.556 |
| P2−P3 | 4.105 |
| P2−P2 | 4.109 |
| P2−P3 | 4.184 |
| P2−P4 | 4.199 |
| P2−P2 | 4.223 |
| P2−P3 | 4.252 |
| P2−P4 | 4.492 |
| P3−P3 | 3.816 |
| P3−P4 | 4.176 |
| P3−P3 | 4.197 |
| P3−P4 | 4.369 |
| P3−P3 | 4.489 |

[a] Units are Å.

**Table 4. Selected Mn−P Bond Lengths for $Ca_{14}MnP_{11}$**

| pair | distance[a] |
|---|---|
| Mn−P2 | 2.5426(8) |
| Mn−P3 | 4.9394(9) |
| Mn−P4 | 5.2089(3) |
| Mn−P3 | 5.3234(9) |
| Mn−P1 | 5.9589(6) |

[a] Units are Å.

the paramagnetic Mn ions and the NMR active $^{31}P$ nuclei. A selection of the shortest Mn−P distances as a function of P site is included in Table 4.

The isotropic $^{31}P$ chemical shift values $\delta_{iso}$ found for $Ca_{14}AlP_{11}$ are shown in Table 1. The −58 to +119 ppm range reflects the metallic character of the material and is consistent with other diamagnetic phosphorus containing materials that display shifts extending from −195 ppm for $Zn_3P_2$ to +146 ppm for GaP. [24−26] To relate the $^{31}P$ MAS spectra for $Ca_{14}AlP_{11}$ shown in Figure 6a to structure, both the intensity and the CSA principal values are necessary parameters. First consider the most intense peaks in these spectra. According to Table 1, both peaks 1 and 4 have relative intensities of four, but peak 4 has a small positive anisotropy $\delta$ = +41 ppm and peak 1 has a large negative anisotropy $\delta$ = −150 ppm. With regards to the structure discussed above for $Ca_{14}AlP_{11}$, these peaks likely correspond to the P3 and P2 sites on the basis of intensity alone. The P2 site contains a chemical bond to Al in the $AlP_4^{9-}$ tetrahedron while the P3 site is isolated in the crystal structure with eight $Ca^{2+}$ nearest neighbors as shown in Figure 2, parts b and a, respectively. Therefore, the P2 site should display a larger anisotropy than the P3 site suggesting that peak 1 and peak 4 in the $^{31}P$ MAS spectra shown in Figure 6a are due to the P2 and P3 sites, respectively. This assignment is consistent with the asymmetry in the chemical shift tensor for peaks 1 and 4 as $\eta$ = 0.2 and 0.9, respectively. The Al−P chemical bond likely introduces some local symmetry at the P2 site forcing $\delta_{11}$ and $\delta_{22}$ to be more similar than $\delta_{33}$, thus producing a small value for $\eta$. The monocapped octahedron of $Ca^{2+}$ ions surrounding the P3 site produces an asymmetric environment yielding a larger $\eta$ value.

Next consider the constituents of the linear anion. As mentioned above this linear anion comprises the P1 and P4 sites. If the linear anion is trimeric, then the $^{31}P$ NMR spectrum should display two peaks in a 2:1 intensity ratio because, with reference to Figure 2c, the P1 sites will be in similar environments and the P4 site will be exactly in the center of the $Ca^{2+}$ cage. On the other hand, if the linear anion is a monomer−dimer combination, the $^{31}P$ NMR spectrum should display three peaks in a 1:1:1 intensity ratio. In this second case the two P1 sites are in different chemical environments thus producing two separate $^{31}P$ NMR peaks. With reference to Figure 6 and Table 1, the $^{31}P$ MAS NMR spectrum is best fit with five peaks, two due to the P2 and P3 sites discussed above and three peaks as yet unassigned. The putative monomer−dimer structure can be immediately discounted on the basis of the NMR data for peaks 2, 3, and 5 because these peaks are in a 2:1:2 intensity ratio and not the anticipated 1:1:1 intensity ratio. The $^{31}P$ NMR results summarized for peaks 2 and 3 in a 2:1 intensity ratio in Table 1 support the idea of a trimeric linear anion. Both peaks display a large anisotropy consistent with the structure in Figure 2c. The large asymmetry for peaks 2 and 3 support the assignment of the P1 and P4 sites, respectively. The eight $Ca^{2+}$ ions surrounding the P1 site in Figure 2c render $\delta_{11} \neq \delta_{22}$ assuming that $\delta_{33}$ lies along the P1−P4 bond. Similarly assuming that $\delta_{33}$ for the P4 site lies along the P1−P4 bond suggests both the absence of motion at room temperature and that the two four-membered $Ca^{2+}$ rings surrounding the P4 site must be puckered because $\delta_{11} \neq \delta_{22}$ in Table 1 for peak 3. Note that if there is either fast motion or ring planarity the off axis principal values would be equal, $\delta_{11} = \delta_{22}$. To further examine the P4 site motion, the sample was cooled to 77 K. As expected there were no $^{31}P$ NMR spectral changes consistent with a static trimer structure. Finally consider peak 5. Depending on reaction batch and or exposure to air, the relative intensity of this peak changes, suggesting that this peak is most likely due to an impurity. One possible impurity could be the compound $P_4O_6$ that resonates at $\delta_{iso}$ = 113 ppm; however, $Ca_{14}AlP_{11}$ apparently decomposes into an amorphous solid, with the elimination of the powder diffraction pattern. This may be attributed to reaction with small amounts of water. This process will be examined in more detail in the future using $^1H-^{31}P$ cross-polarization.

All spectral assignment for $Ca_{14}AlP_{11}$ has thus far been based on fitting the observed $^{31}P$ MAS NMR spectra in Figure 6a to a superposition of CSA powder patterns. In reality, however, there are both $^{27}Al-^{31}P$ and $^{31}P-^{31}P$ dipolar and scalar couplings. Indeed the severe 20 ppm line widths in Figure 6a at all spinning speeds suggest operation of one, both, or other nonrelaxation-based line broadening mechanisms. The possibility of $^{27}Al-^{31}P$ heteronuclear couplings causing the line broadening can be eliminated as decoupling $^{27}Al$ during excitation and detection as well, since $^{27}Al$ irradiation in one window of a $^{31}P$ spin echo experiment did not alter the $Ca_{14}AlP_{11}$ $^{31}P$ NMR spectra. The decay of the $^{31}P$ spin echo for the compound $Ca_{14}AlP_{11}$ with and without rotor synchronized MAS suggests that $^{31}P-^{31}P$ dipolar couplings could be corrupting the $^{31}P$ NMR signal ultimately producing the abnormally broad $^{31}P$ MAS NMR spectra in Figure 6a. The decay of the spin echo without MAS is due to $^{31}P-^{31}P$ dipolar coupling, whereas this decay mechanism is removed by rotor synchronized MAS as demonstrated by the solid diamonds and triangles in Figure 7, respectively. The decay of the $^{31}P$ spin echo in Figure 7 for static $Ca_{14}AlP_{11}$ is a good measure of the $^{31}P-^{31}P$ distance in the Zintl structure. The functional form of the static spin echo decay $I(2\tau)/I(0)$ for homonuclear dipolar coupled systems can be related to the second moment of a distribution of dipolar couplings at the $j$th site $M_{2d}^{(j)}$ as

$$\frac{I(2\tau)}{I(0)} = \prod_j a_j \exp\left[-\frac{(2\tau)^2}{2} M_{2d}^{(j)}\right] \qquad (1)$$

(24) Gibby, M. G.; Pines, A.; Rhim, W.-K.; Waugh, J. S. *J. Chem. Phys.* **1972**, *56*, 991.
(25) Nissan, R. A.; Vanderah, T. A. *J. Phys. Chem. Solids* **1989**, *50*, 347.
(26) Sears, R. E. J. *Phys. Rev. B.* **1978**, *18*, 3054.

**Table 5. Second Moments for Each P Site in $Ca_{14}AlP_{11}$**

| site | $j$ | $M_{2d}^{(j)}$ [a] |
|---|---|---|
| P1 | 1 | 27 |
| P2 | 2 | 13 |
| P3 | 3 | 12 |
| P4 | 4 | 41 |

[a] Units are $10^6$ rad$^2$/s$^2$.

where $\tau$ is the spacing of the 90 and 180° rf pulses and $a_j$ is the spectral intensity of the $j$th site. According to Van Vleck,[27] the second moment of a distribution of dipolar couplings for the $j$th site $M_{2d}^{(j)}$ can be related to the distance between nuclei $r_{ij}$ as

$$M_{2d}^{(j)} = \frac{3}{5}\left(\frac{\mu_0}{4\pi}\right)^2 \gamma^4 \hbar^2 I(I+1) \sum_{i>j} \frac{1}{r_{ij}^{\,6}} \qquad (2)$$

where $\gamma$ is the gyromagnetic ratio, $I$ is the spin quantum number, $\mu_0$ is the magnetic permeability, and $\hbar$ is Planck's constant. The second moments for the distribution of $^{31}P-^{31}P$ distances for $Ca_{14}AlP_{11}$ within 5 Å were calculated from Table 3 and eq 2 and are shown in Table 5. Insertion of these values into eq 1 yields the dashed line shown in Figure 7, a curve in good agreement with the experimental results shown in Figure 7. One major difference between theory and experiment is that the experimental decay in Figure 7 suggests an exponential rather than Gaussian spin echo decay. Typically such behavior is observed in the presence of structural dynamics, however, this contention is in disagreement with the lower temperature MAS experiment mentioned above.

Although an Al−P distance cannot be measured from the $^{31}P$ NMR results in Figures 6 and 7 because the effect of the $^{27}Al$ nucleus is not clearly manifest in the $^{31}P$ NMR spectra, structural distortion information about the $AlP_4^{9-}$ tetrahedron can be obtained from the $^{27}Al$ NMR data in Figure 8. To begin with, the $^{27}Al$ chemical shift of 180 ppm is more positive than most oxides,[28] however, it is in quite good agreement with shifts in other III−V semiconductors like AlN, AlP, and AlAs.[29,30] In special cases where small band gaps are present large paramagnetic shifts can be observed as for example in $Al_2Ru$ where a 313 ppm $^{27}Al$ chemical shift has been reported.[31] On the basis of shift alone, one would expect the band gap in $Ca_{14}AlP_{11}$ to be smaller than the standard Al containing III−V semiconductors. The splitting in the $^{27}Al$ NMR spectra in Figure 8 is consistent with X-ray data, indicating that the $AlP_4^{9-}$ tetrahedron is slightly compressed along the $z$-axis thus destroying the spherical symmetry about the $^{27}Al$ nuclear spin. It can be shown that for such an axially symmetric distortion the central $+^1/_2 \rightarrow -^1/_2$ transition for an $I > {}^1/_2$ nucleus in a static sample displays a powder pattern with two singularities or peaks separated by[32]

$$\Delta\nu_Q = \frac{\nu_Q^{\,2}}{16\nu_0}\left(I(I+1)+\frac{3}{4}\right) \qquad (3)$$

where $\Delta\nu_Q$ is the splitting of the quadrupole doublet, $\nu_Q$ is the quadrupolar coupling constant, and $\nu_0$ is the Larmor frequency. In the special case of the $I = {}^5/_2$ $^{27}Al$ nucleus, $\Delta\nu_Q = 19\nu_Q^2/32\nu_0$. The $^{27}Al$ NMR data in Figure 8 agree with eq 3. The lower magnetic field splitting of 32.8 ppm in Figure 8a is greater than the higher field splitting of 23.3 ppm in Figure 8b because of the Larmor frequency scaling factor in the denominator of eq 3. Converting these splittings into frequency units and comparing to eq 3 yields $\nu_Q = 742$ kHz for the low magnetic field spectrum and $\nu_Q = 626$ kHz for the high magnetic field spectrum. The discrepancy between these values is probably caused by the fact that the spectra are also affected by the asymmetry parameter $\eta$, which determines the deviation from perfect axially symmetry in this compressed tetrahedron. To interpret the spectra a mean value of $\nu_Q \approx 700$ kHz is chosen. In the case of a perfectly spherical environment $\nu_Q = 0$ because the field gradient $V_{zz} = 0$. Since in the case of $^{27}Al$ $\nu_Q = 6 \times 10^7 V_{zz}$, the field gradient at the $^{27}Al$ nucleus becomes $V_{zz} = 1.16 \times 10^{12}$ V/m$^2$ which implies a fairly large electric field $E = 295$ V/m given the Al−P distance of about 2.54 Å. Barring other strain mechanisms in the powdered solid, this field gradient is indicative of the $z$-axis distortion predicted by single-crystal X-ray data.[18,19]

Assignment of the $^{31}P$ wide line NMR spectrum of $Ca_{14}MnP_{11}$ in Figure 9 is aided by consideration of the spin lattice relaxation data shown in Figure 10. The $T_1$ values extracted from Figure 10 for $Ca_{14}MnP_{11}$ lie in four discrete regions as shown in Table 2. The raw $^{31}P$ NMR data in Figure 9a can be essentially deconvolved with the rf excitation bandwidth to yield an approximation to the true spectrum for $Ca_{14}MnP_{11}$ in Figure 9b. As mentioned above, this synthetic spectrum is well described by four Gaussians with position, intensity, and width given in Table 2. The assignment of peaks 1, 2, 3, and 4 as the P4, P3, P1, and P2 sites is consistent with the Gaussian intensities in Table 2. Peak 4 representing the P2 site is the closest to the Mn ion and displays the smallest $T_1$ value and the largest shift difference with respect to the $Ca_{14}AlP_{11}$ values. The factor of 2 difference in the width of peaks 2 and 3 for the P3 and P1 site respectively is consistent with the factor of 2 difference in the $T_1$ values. Both the trend in $T_1$ and shift for the assignment of these two peaks is inconsistent with the distances in Table 4 since the Mn−P3 distance is less than the Mn−P1 distance. Indeed, the assignment of peak 1 to the P4 site is also inconsistent with the distances in Table 4. On the basis of distance, shift, and $T_1$ value one would assign the peaks 1, 2, 3, and 4 to the P1, P4, P3, and P2 sites, respectively, and not the P4, P3, P1, and P2 intensity-based trend mentioned above. This inconsistency means that

(27) Van Vleck, J. H. *Phys. Rev.* **1948**, *74*, 1168.
(28) Oestrike, R.; Navrotsky, A.; Turner, G. L.; Montez, B.; Kirkpatrick, R. J. *Am. Mineral.* **1987**, *72*, 788. Massiot, D.; Bessada, C.; Coutures, J. P.; Taulelle, F. *J. Magn. Reson.* **1990**, *90*, 231. Smith, M. E.; Jaeger, C.; Schoenhofer, R.; Steuernagel, S. *Chem. Phys. Lett.* **1994**, *219*, 75; Mundus, C.; Mueller-Wahrmuth, W. *Solid State Nucl. Magn. Reson.* **1995**, *5*, 79. Wölker, A.; Hudalla, C.; Eckert, H.; Auroux, A.; Occelli, M. L. *Solid State Nucl. Magn. Reson.* **1997**, *9*, 143.
(29) Sears, R. E. J.; *Phys. Rev. B.* **1980,** *22*, 1135.
(30) Han, O. H.; Timken, H. K. C.; Oldfield, E.; *J. Chem. Phys.* **1988**, *89*, 6046.
(31) Hill, E. A.; Volkov, P.; Poon, S. J.; Wu, Y.; *Phys. Rev. B.* **1995**, *51*, 4865.
(32) Kundla, E.; Samoson, A.; Lippmaa, E.; *Chem. Phys. Lett.* **1981**, *83*, 229.

the electron is not completely localized on the Mn ion at room temperature and that for large Mn−P distances, the electron−$^{31}$P interaction is dominated by contact or through bond interactions not dipolar or through space interactions. To be completely certain of the peak assignment for the $^{31}$P NMR spectrum of $Ca_{14}MnP_{11}$, a detailed comparison of the chemical shift and relaxation data with the electronic band structure must be accomplished.

To test the idea of electron delocalization in the $Ca_{14}MnP_{11}$ compound, the EPR spectra down to 25 K were obtained. The spectra shown in Figure 11a are consistent with those of a free electron at $g = 2$ without hyperfine couplings to either $^{55}$Mn or $^{31}$P nuclei. The lack of $^{55}$Mn hyperfine couplings at all temperatures suggests that either the electron is not localized on the Mn ion in $Ca_{14}MnP_{11}$ as expected from the $^{31}$P wide line NMR data mentioned above or that the EPR spectra for $Ca_{14}MnP_{11}$ are severely exchange broadened. In either case, a band structure calculation is needed to understand the NMR parameters in $Ca_{14}MnP_{11}$. Finally, the magnetoresistive $Eu_{14}MnP_{11}$ compound was examined by wide line $^{31}$P NMR and EPR. The ≈4 MHz wide $^{31}$P NMR spectrum separates into four spectral regions much like those shown in Figure 9 for the $Ca_{14}MnP_{11}$ compound and again a preliminary spectral assignment can be made. However, due to the lack of detailed structure calculations and the added feature of a magnetic phase transition at 52 K, this discussion is omitted. A clue into the phase behavior of the $Eu_{14}MnP_{11}$ compound can be obtained from the EPR spectra in Figure 11b. As the 52 K transition temperature is reached, the EPR spectrum shifts to lower field and displays hyperfine couplings. Below 47 K, the EPR spectrum completely disappears consistent with the ferromagnetic state. The 374 G hyperfine coupling present in the 51 and 49 K data suggests that the transition from the paramagnetic to ferromagnetic state involves electron localization. The derivative of these two spectra reveals three clear peaks at 51 K and six peaks at 47 K consistent with localization on either $I = {}^5/_2$ $^{55}$Mn or $^{151}$Eu nuclei. It has been suggested that ferromagnetism in Zintl phases involves ordered Mn sites, and this result is consistent with that hypothesis. However, the EPR data alone cannot distinguish between magnetic ordering of $^{55}$Mn or $^{151}$Eu. Probably the most important observation of this measurement is that if the localization is due to Mn, then it is most likely present as $Mn^{2+}$. This model would require that Mn be high-spin $Mn^{2+}$ that is antiferromagnetically coupled to an unpaired spin delocalized over the four Pn atoms in the tetrahedron.[16,17] Overall, the total charge for the unit, $MnP_4^{9-}$ is preserved and the magnetic susceptibility would be consistent with four unpaired spins.

## Conclusions

The isostructural series of compounds, $Ca_{14}MnP_{11}$, and $Eu_{14}MnP_{11}$ were studied with magnetic resonance. Variable spinning speed $^{31}$P MAS NMR spectra for $Ca_{14}AlP_{11}$ suggest that the P1−P4−P1 linear anion in the Zintl structure is trimeric at room temperature in contrast to IR measurements on $Ba_{14}AlP_{11}$. Both wide line $^{31}$P NMR and EPR spectra for the $Ca_{14}MnP_{11}$ compound suggest electron delocalization down to 25 K. Finally, the 374 G hyperfine coupling in the EPR spectrum of $Eu_{14}MnP_{11}$ near the 52 K paramagnetic to ferromagnetic phase transition temperature suggests electron localization on either the Mn or the Eu sites in the Zintl structure.

**Acknowledgment.** Portions of this work were supported by a UC Davis Young Faculty Award, by the donors of the Petroleum Research Foundation, administered by the American Chemical Society, and the National Science Foundation through Grant Nos. CHE-9984654 and DMR-9803074. M.P.A. is an Alfred P. Sloan and a David and Lucile Packard Fellow. We thank Amy Payne for her contributions to the early part of this work, Ray Carter for help with the Herzfeld−Berger analysis, and Brian Phillips for the use of the W. M. Keck Solid State NMR facilities.

CM010809Q

(33) Duncan, T. M. *A Compilation of Chemical Shift Anisotropies*; The Farragut Press: Chicago, IL, 1990.